AIP Advances

Temperature dependence of the anomalous Nernst coefficient for $Ni_{80}Fe_{20}$ determined with metallic nonlocal spin valves

Cite as: AIP Advances **10**, 065127 (2020); https://doi.org/10.1063/5.0006599
Submitted: 05 March 2020 • Accepted: 30 May 2020 • Published Online: 19 June 2020

R. K. Bennet, A. Hojem and B. L. Zink

Temperature dependence of the anomalous Nernst coefficient for $Ni_{80}Fe_{20}$ determined with metallic nonlocal spin valves

Cite as: AIP Advances 10, 065127 (2020); doi: 10.1063/5.0006599
Submitted: 5 March 2020 • Accepted: 30 May 2020 •
Published Online: 19 June 2020

R. K. Bennet, A. Hojem,[a] and B. L. Zink[b]

AFFILIATIONS

Department of Physics and Astronomy, University of Denver, Denver, Colorado 80208, USA

[a]**Present address:** Department of Physics, University of California San Diego, La Jolla, CA 92093-0354, USA.
[b]**Author to whom correspondence should be addressed:** barry.zink@du.edu

ABSTRACT

The anomalous Nernst effect, which generates an out-of-plane charge voltage in response to a thermal gradient perpendicular to the magnetization of a ferromagnet, can play a significant role in many spintronic devices where large thermal gradients exist. Since they typically include features deep within the submicron regime, nonlocal spin valves can be made very sensitive to this effect by lowering the substrate thermal conductance. Here, we use nonlocal spin valves suspended on thin silicon nitride membranes to determine the temperature dependence of the anomalous Nernst coefficient of 35 nm thick permalloy ($Ni_{80}Fe_{20}$) from 78 K to 300 K. In a device with a simple ferromagnet geometry, the transverse Seebeck coefficient shows a weak temperature dependence, with values at all T near 2.5 μV/K. Assuming previously measured values of the Seebeck coefficient for permalloy, which has a near-linear dependence on T, leads to a low temperature upturn in the anomalous Nernst coefficient R_N. We also show that the temperature dependence of this coefficient is different when a constricted nanowire is used as the ferromagnetic detector element.

I. INTRODUCTION

In nanoscale spintronic circuits, large charge current densities can create large thermal gradients that impact the resulting signal through various thermoelectric and thermal spin effects. It is vital to understand how material choices and device construction can enhance or suppress these effects to achieve a sufficient signal-to-noise ratio in upcoming industrial applications. One important example of such a magnetothermoelectric effect is the anomalous Nernst effect (ANE). Whenever a significant portion of the thermal gradient is perpendicular to the magnetization of a ferromagnetic element of a device, the ANE can contribute significantly to the observed spin signal.[1–5]

Often described as the thermal analog to the anomalous Hall effect,[3] the ANE arises when a thermal gradient ∇T is perpendicular to the magnetization $\hat{m}$ of a ferromagnet, producing a mutually perpendicular electric field ∇V, as shown in Fig. 1(a). This electric field is given by the equation

$$\nabla V_N = -S_N \hat{m} \times \nabla T, \quad (1)$$

with $\hat{m}$ in the direction of the magnetization of the FM and ∇T being the thermal gradient across the contact. Here, S_N is the transverse Seebeck coefficient, which is often expressed as $S_N = R_N S_{FM}$, where R_N is termed the anomalous Nernst coefficient and S_{FM} is the absolute Seebeck coefficient of the ferromagnet.

Despite the importance of material-dependent parameters like R_N, as well as similar studies conducted on anomalous Hall resistivity,[6–8] the temperature dependence of the anomalous Nernst coefficient of thin films or nanostructures of permalloy (Py, the Ni–Fe alloy with 80% Ni) has not been reported to our knowledge, although other techniques have been used to investigate T-dependence of the ANE for other materials.[9,10] Indeed, a relatively fewer number of reports investigate room temperature behavior of the ANE

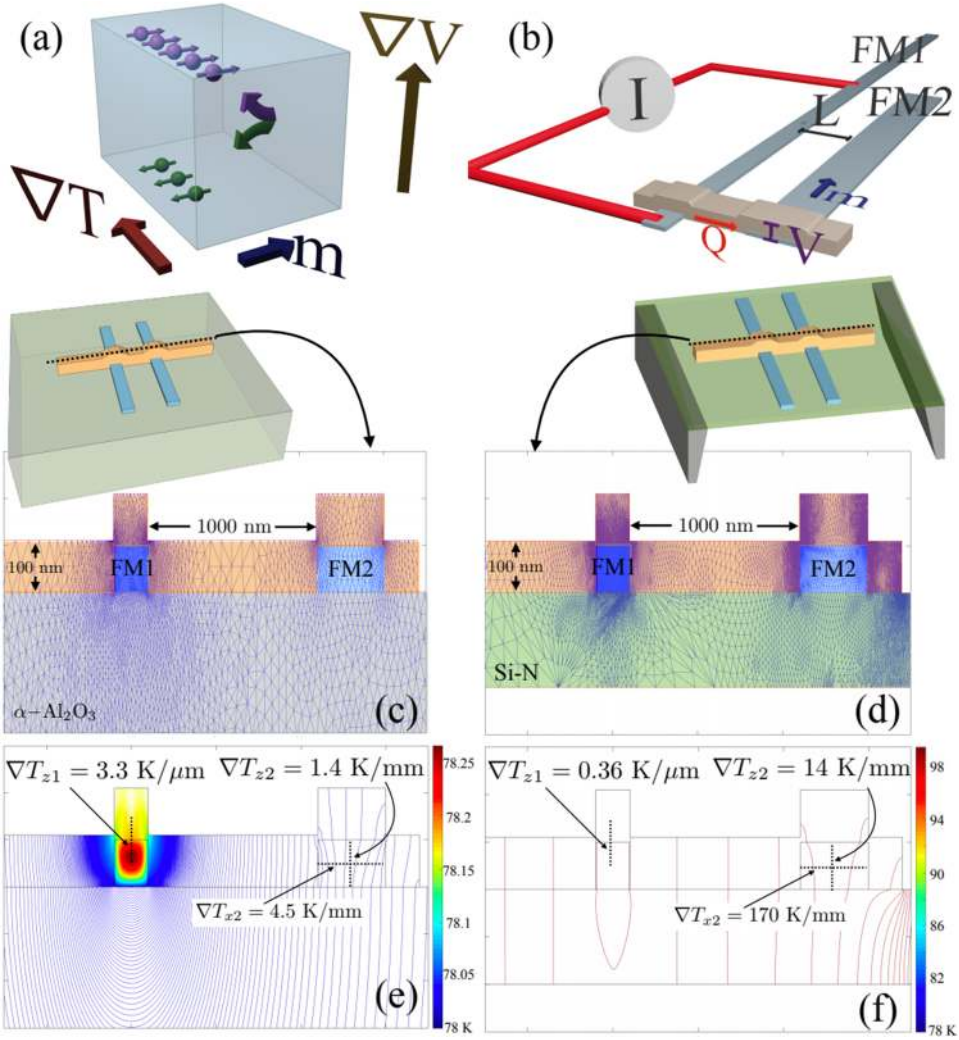

FIG. 1. (a) Schematic view of the ANE exhibited in a ferromagnet. In response to a lateral thermal gradient ∇T perpendicular to the magnetization m, an out-of-plane electric field ∇V is formed, (b) a schematic illustrating ANE generation in an NLSV using thermal spin injection. The charge current I, heat flow Q, magnetization m, voltage gradient V, and FM separation length L are indicated, (c) the cross-sectional FEM model mesh and geometry for an NLSV using Py and Al formed on a single-crystal sapphire substrate. Note the substrate extends far below the view shown here, (d) a similar FEM model mesh and geometry, with the bulk substrate removed in favor of a suspended Si–N membrane, and [(e) and (f)] calculated T for the two models, where the power dissipated in FM1 is 16× lower for the membrane case to roughly match the applied currents used. ∇T is indicated for selective areas, showing the large enhancement of in-plane ∇T driven by the removal of the bulk heat sinks of the substrate.

in permalloy.[2,11] Considering the ubiquity of Py in spintronic and spin caloritronic devices, as well as the impact of anomalous Nernst effects on these structures,[11–18] an improved understanding of the temperature dependence of the ANE in permalloy is valuable to both spintronic and spin caloritronic efforts. Here, we engineer nonlocal spin valves (NLSVs, also known as lateral spin valves) to maximize the in-plane thermal gradient and enhance and isolate the ANE.

We use NLSVs for their unique ability to separate charge current from pure spin current.[19–23] Spin is injected into a non-magnetic metallic nanowire by applying a charge current to one ferromagnetic nanowire under an in-plane external magnetic field H. The charge current is shunted away from the detector FM, which is separated from the injector FM by a distance L limited by the spin diffusion length λ_{NM} of the non-magnetic metal, and the pure spin current diffuses down the NM channel. It is detected at the second FM as a nonlocal voltage.

Recently, NLSVs have emerged as an important tool in the growing field of spin caloritronics, which studies coupling between heat and spin in materials and devices,[24–26] since the ANE and other thermal and thermoelectric effects dominate the background nonlocal resistance of NLSVs.[11,27,28] Figure 1(b) illustrates how the ANE arises in our NLSVs when the charge current I is driven through one of the ferromagnetic nanowires, FM1. Pure spin current diffuses down the nonmagnetic channel, along with the heat Q that gives rise to an in-plane thermal gradient. The out-of-plane voltage gradient V due to the ANE is generated in the detector, FM2, in response to this applied in-plane gradient.

The ANE portion of the NLSV response can be enhanced by dramatically decreasing the substrate thermal conductance such that the majority of the thermal gradient produced by the high charge current density in the injector nanowire lies in the plane of the detector FM magnetization. We demonstrated this in a previous work by fabricating NLSVs on thin amorphous silicon-nitride

(Si–N) membranes with very low thermal conductance,[29] and we now show a simple model demonstrating this effect in Figs. 1(c)–1(f). Here, we use 2D finite element analysis of the heat flow, described in greater detail in Sec. III, in two simplified NLSVs. One NLSV is supported on a 500 μm thick bulk sapphire (α–Al_2O_3) substrate, and the second is formed on a 500 nm thick suspended Si–N membrane, fabricated by removing the bulk Si beneath the Si–N membrane using an anisotropic bulk Si etch, as described in more detail elsewhere.[29] These cross-sectional models assume that the central 450 nm of the NM channel, indicated with the dashed line in the inset schematics, has uniform heat, charge, and spin flow, and so do not give quantitatively accurate thermal gradients. However, they clarify the qualitative concept we use in our ANE measurements. Figures 1(c) and 1(d) show the simple cross-sectional geometry with a false color overlay for the substrate and membrane-supported NLSV, respectively, along with the mesh used in the model calculation. Here, thermal conductivity values for FM, NM, and Si–N are taken from previous measurements,[29–31] and that for sapphire is taken from the literature.[32] We show example calculations of the temperature as a function of position in panels (e) and (f). These already make clear that the strongest gradients for the substrate case are predominately out-of-plane (labeled ∇T_z) and near FM1 where heat is applied to the model. In stark contrast, the dominant thermal gradients in the membrane case are in-plane (labeled ∇T_x), as well as much more uniform, as expected by the removal of the bulk heat sink beneath the thin film structures.[12,33–36] We also note that the temperature is elevated by ~20 K for the membrane case, despite using a modeled heating power 16× lower than that used for the substrate case. This is also unsurprising in light of the removal of the bulk substrate. We also indicate calculated values of thermal gradients for these conditions at key locations, which show that the membrane-supported NLSV has approximately one order of magnitude lower ∇T_z at the heated FM1/NM interface, while keeping a 38× higher ∇T_x across the detector FM2. This provides our rationale for using the Si–N membrane NLSVs to study the ANE as a function of temperature since the relative reduction of ∇T_z reduces thermal spin injection, or the spin dependent Seebeck effect (SDSE),[30,37–42] and allows us to record large ANE signals from NLSVs. The nearly two-dimensional nature of the circuits also allows us to simplify our analysis by performing 2D finite-element modeling to calculate the in-plane thermal gradients. This is a distinct advantage since determining the thermal gradient in nanoscale circuits or thin films is often the most significant challenge. This modeling, which we performed at a single temperature in an earlier publication, uses values of thermal conductivity vs T measured using other Si–N membrane techniques on similar thin film structures.[31,43]

In this paper, we use this combination of extreme thermal isolation and 2D modeling of thermal gradients to determine the temperature dependence of R_N for Py. We also present evidence that NLSV circuit geometry has a significant and unusual effect on the relative thermal profiles across the detector contacts.

II. EXPERIMENTAL DETAILS

As described in a previous work,[29] we photolithographically pattern platinum electrical contact leads on 500 μm thick Si–N coated Si wafers and then use SF_6 plasma etch to form cleave marks for 1 × 1 cm^2 chips and windows in the Si–N on the back of the wafer, exposing the bulk Si. We then etch the bulk Si in 60% tetramethyl ammonium hydroxide (TMAH) at 95 °C for 10 h to form 90 × 90 μm^2 Si–N membranes.

Using a two-step electron-beam lithography process,[30] we then fabricate NLSVs on these Si–N membrane windows using Py and Al. The deliberate variance in size and shape between FM1 and FM2, as shown in Fig. 1(b), creates different switching fields for the two strips when an external field is applied to the plane of the strips. Via e-beam evaporation, we deposit 35 ± 5 nm Py at ≈0.1 nm/s in a load-locked UHV chamber with a typical base pressure of $\ll 10^{-8}$ Torr and aluminum in a high-vacuum chamber at a higher rate of ≈0.5 nm/s–1 nm/s. The Py forms a native oxide due to exposure to atmosphere during this two-step process, and although we perform an Ar RF-cleaning step immediately prior to deposition of the aluminum layer, we do not believe that this would be sufficient to remove the native Py oxide. Our previous work shows that the oxide does reduce overall signal size under electrical spin injection but does not inhibit thermal spin injection.[30]

We produced devices with the intended L = 500 nm and L = 800 nm on Si–N membranes on two different chips using the same metal deposition steps to minimize variations in material quality. Both use a uniform 200 nm intended width of FM1. The L = 500 nm device uses a uniform geometry for FM2 with a constant width of ≈400 nm, while the L = 800 nm device narrows from 500 nm to 200 nm at the junction between the FM detector and the NM channel to produce a contact area of 200 × 300 nm^2, the same as that of the FM injector/NM channel junction. We study each NLSV in two orientations (A and B), where the FM strips change roles from spin injector to detector, which also reverses the direction of ∇T in the spin channel. Furthermore, we inject spin in two different ways. In the standard electrical spin injection, charge current enters an FM and is extracted from the NM contact away from the spin channel. In thermal spin injection, the current I_t passes only through the FM such that Joule heat introduces a large thermal gradient that drives spin into the channel via the spin dependent Seebeck effect (SDSE)[37] and generates thermal gradients at the detector that leads to the ANE.

It is fairly common to measure NLSVs using AC techniques with a lock-in amplifier. In that approach, authors often measure the signal component proportional to the excitation frequency ω and that proportional to 2ω and assume the latter contains information related to thermal effects since Joule heating is proportional to I^2.[11,39,41,44] As in our earlier work,[29,30] as well as that of some other groups,[45,46] here, we have chosen to use quasi-DC measurement of the entire IV curve for the NLSV, made by integrating differential conductance curves using a Keithley 6221 precision current source and a 2182a nanovoltmeter. Fitting this curve gives the electrically-driven components proportional to I and the thermally driven components proportional to I^2 directly. We identify the switching locations of each NLSV at each T by recording the non-local R using the "delta-mode" DC reversal technique with the same equipment. Note that to avoid confusion with the Nernst coefficient, we use the term R in this paper to refer to the non-local measurement, $R = V_{nl}/I$. All R presented here are such non-local measurements. The fit coefficients of IV curves are then referred to as R_1 and R_2, where the field operating point is indicated with a sub-script or parentheses.

III. RESULTS AND DISCUSSION

Figure 2 presents example measurements and schematic R vs H diagrams to overview the measurement techniques used to determine the ANE contributions to the NLSV signal. We first focus on the electrical spin injection case in orientation B for the L = 500 nm device, shown schematically at the top left. Figure 2(a) shows an example R vs H sweep which we use to determine the field operation points for subsequent IV curve measurements. This shows a fairly typical NLSV response, and although this case does not isolate thermal effects, a small hysteresis contribution that originates in the ANE is already visible. This non-local voltage contribution is due to the large in-plane thermal gradients that are formed, which allow Peltier effects proportional to I to also generate small thermal gradients and drive a signal component $\propto I$. To isolate thermal effects that result from either electrical spin injection or thermal spin injection, we measure the full IV response at selected magnetic fields. An example is shown in Fig. 2(b), which compares a small region of the full IV response for the two full saturation points (here ±400 Oe), which we identify as the parallel point on the positive field branch, P_p, and the parallel point on the negative field branch, P_n. The full IV curve is shown in the inset. This curve is dominated for this membrane-supported NLSV by large Seebeck and Peltier terms that are field-independent.

The table below the schematic at the left of Fig. 2 indicates the scheme for isolating spin effects either with or without contributions from the ANE. Fitting the IV curve (or the dV/dI curve before integration) after directly subtracting the data for the appropriate field point allows examination of spin and ANE contributions. We perform a second-order fit $V_{nl} = R_1 I + R_2 I^2$, which yields the contribution due to electrical spin injection and Peltier effects, R_1, and the much more significant contribution due to Joule heating, R_2. As explained in more detail elsewhere,[29] the net contribution due to Joule heating is given by $R_{2,\mathrm{ANE}} = [R_2(\mathrm{P_p}) - R_2(\mathrm{P_n})]/2$.

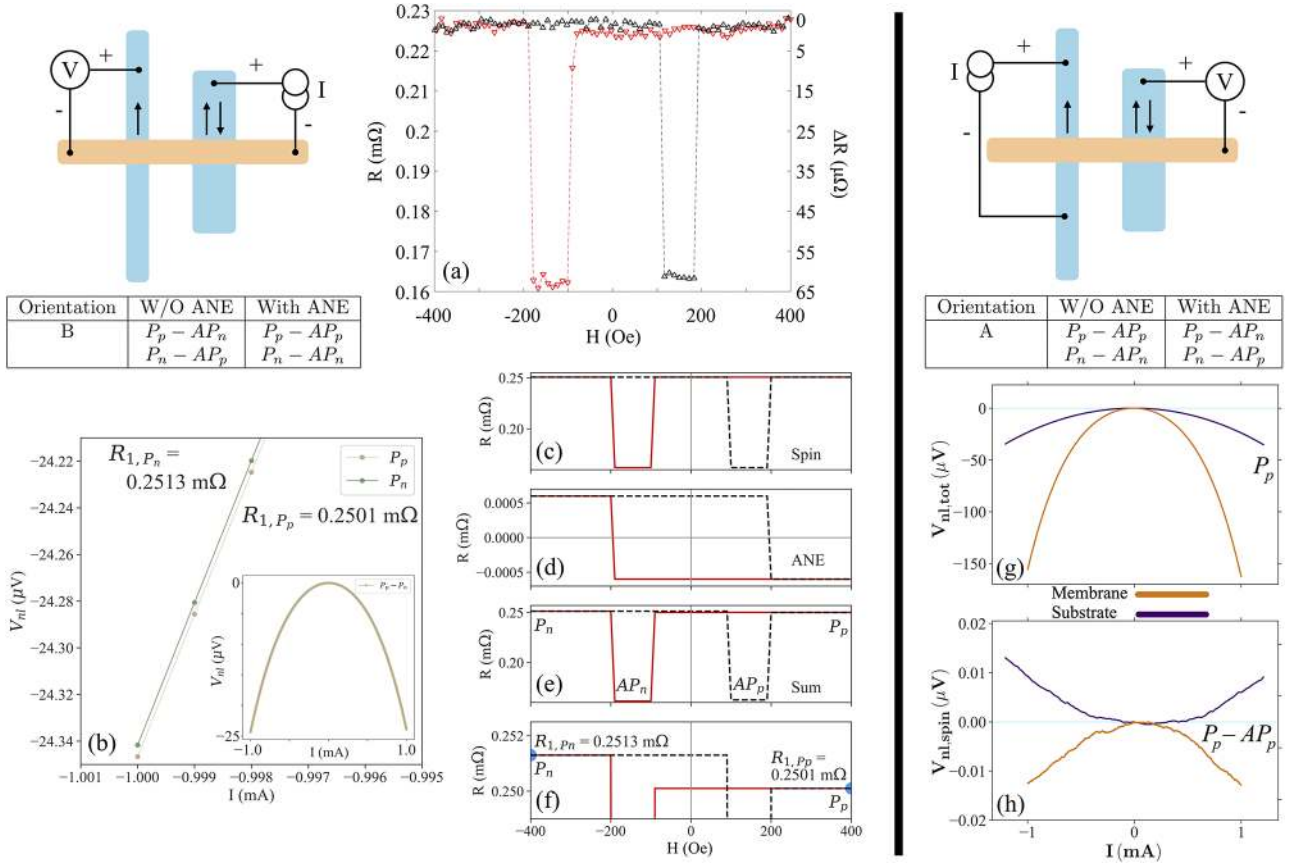

FIG. 2. (a) Non-local R vs H for L = 500 nm NLSV at T = 78 K in orientation B and electrical spin injection, with a small odd signal in applied H visible even at this reduced T (resulting in low S_{FM}), (b) IV curves collected at the parallel-positive (P_p = 400 Oe) and parallel-negative (P_n = −400 Oe) field points plotted from I = −1 mA to I = −0.995 mA, with the inset showing the behavior of the P_p IV curve across the entire measured range of I = −1 mA to I = 1 mA. Linear fits to each IV curve are annotated and agree well with the R values in (a); small variations are due to the more precise IV measurement than used for the R vs H sweeps, [(c)–(f)] illustration of the addition of an ANE signal (d) to the characteristic spin-switching signal of the NLSV (c). This results in a small asymmetry between the up-sweep (black, dashed) and down-sweep (red, solid) visible in (e), shown in greater detail in (f). The field switching points at which we collect more detailed IV curves—parallel-positive (P_p), parallel-negative (P_n), antiparallel-positive (AP_p), and antiparallel-negative (AP_n)—are indicated in (e), and the final non-local resistance values R_1 at P_p and P_n are shown in (f), and (g) raw and (h) spin-isolated IV curves for substrate-supported (dark purple) and membrane-supported (orange) L = 500 nm devices in orientation A at a bath temperature of 200 K.

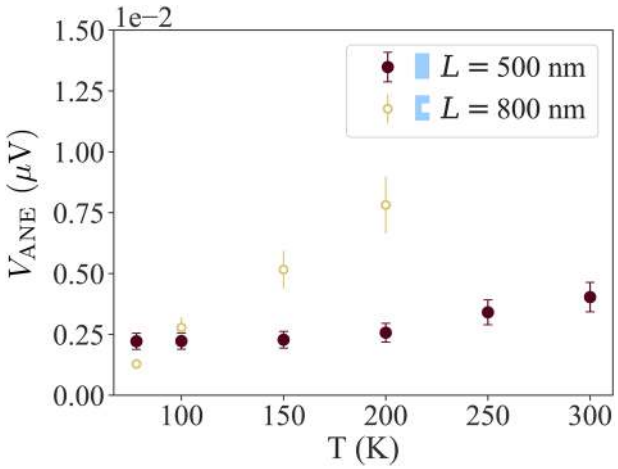

FIG. 3. Anomalous Nernst voltage V_{ANE} due to Joule heating for an applied current of 274 μA, plotted as a function of bath temperature T for L = 500 nm (red closed circles) and L = 800 nm (open yellow circles). The L = 800 nm device shows strong temperature dependence.

This allows us to calculate the Nernst voltage $V_{ANE} = R_{2,ANE}I^2$ at a given I.

Figures 2(c)–2(f) overview the two main components to the NLSV response. Figure 2(c) shows the typical spin signal, which is even in field, with the overall magnitude modeled by the 78 K response for the 500 nm NLSV. Figure 2(d) shows the ANE contribution with hysteretic field dependence, with the switching points aligned with the coercive field of the detector FM. The sum of these two is shown in panels (e) and (f), with the relevant field points named in (e) and a closer view shown in (f) along with blue points that indicate the R_1 values determined from the IV fitting procedure. This method of determining the ANE contributions focuses on acquiring the most critical data to accurately determine the ANE and avoids long-term thermal and field drift that arise when measuring the full H dependence of the R_2 response.

The right panels of Fig. 2 focus on the thermal spin injection case in orientation A, as shown schematically at the top right, with the table indicating the scheme for isolating ANE contributions using the field symmetry in this orientation with a reversed in-plane ∇T. In panel (g), we compare the total measured IV curve for the membrane and substrate-supported NLSVs recorded at 200 K, and in panel (h), we compare the spin component of the signal. As previously observed for substrate-supported NLSVs,[30] the full IV curve in the thermally-driven case is already strongly parabolic, and the isolated spin signal also shows a parabolic response indicating the SDSE. The membrane-supported NLSV has even stronger background terms but a smaller spin-isolated signal due to the proportionally smaller out-of-plane gradient needed to generate large SDSE contributions. Finally, note that the spin-isolated IV curves do not contain any contributions from the anomalous Nernst effect (ANE).

The ANE contribution to the signal from an NLSV is given by $V_{ANE} = R_{2,ANE}I^2$, where I is the charge current applied to the thermal spin injection configuration. In Fig. 3, we show V_{ANE} vs T for each device at an applied current I = 274 μA. Similar ANE signals are generated in the electrical spin injection configuration, but as described below, the flow of current from the FM to the NM introduces Peltier effects that complicate the determination of ∇T. The L = 500 nm NLSV has a T independent total ANE voltage contribution roughly below 200 K, with an increase at higher T, while the L = 800 nm device shows a stronger T dependence below 200 K. This device failed before complete data could be acquired at higher T. Note also that without accurate information on the thermal gradient at locations where the detector FM contributes ANE signals, the physical trends in the ANE coefficient cannot be extracted.

To determine the required thermal gradients for our essential 2D membrane structure, we use a commercially available software package[47] for 2D FEM at five base T ranging from 78 K to 300 K for both NLSVs under thermal spin injection and orientation A, using nominal geometry measurements. No models are created for the L = 800 nm NLSV above 200 K as the device failed before reliable data could be collected at these temperatures. These models solve the 2D heat flow equation in steady state,

$$\frac{\partial}{\partial x}\left(k_{2D}(x,y)\frac{\partial T(x,y)}{\partial x}\right)+\frac{\partial}{\partial y}\left(k_{2D}(x,y)\frac{\partial T(x,y)}{\partial y}\right)=P_{2D}(x,y), \tag{2}$$

where $k_{2D} = k \cdot t$ with k being the thermal conductivity (in W/m K) of the NLSV components and t being the thickness of the films.

For most studies that attempt to quantify the thermal gradients in spintronic or spincaloritronic devices, determining the correct thermal conductivity for the thin films and nanostructures used to construct the device is a major challenge. It is not uncommon for authors to use tabulated values of bulk thermal conductivity, which should not be expected to represent the behavior of thin film components with unavoidable higher levels of defects, grain boundaries, and other non-idealities. The use of the Si–N membrane and the resulting 2D nature of the heat transport simplifies this somewhat,

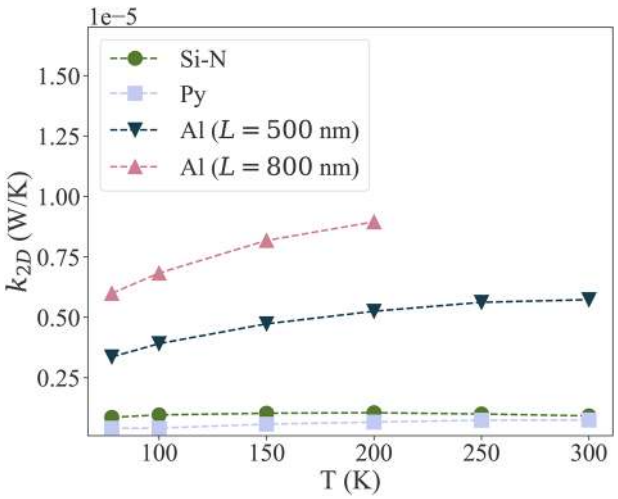

FIG. 4. k_{2D} vs T for the 500-nm Si–N membranes (green circles),[43] Py thin films (light blue squares),[31] and Al thin films.

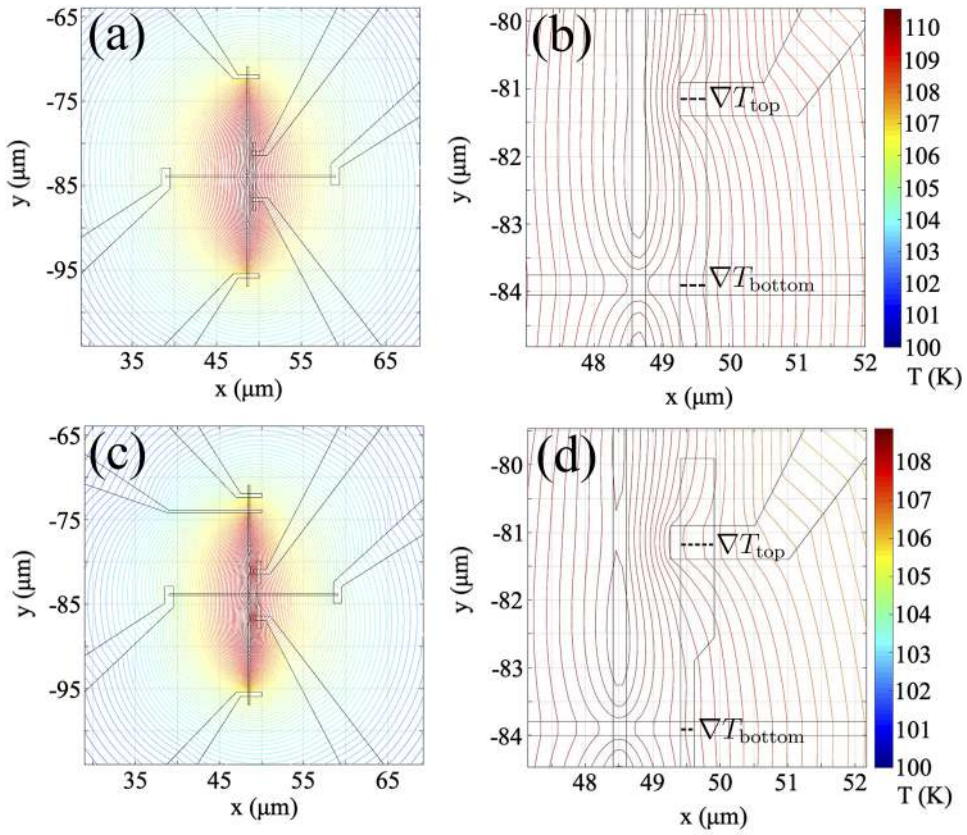

FIG. 5. 2D finite-element modeling for [(a) and (b)] L = 500 nm, (c) L = 800 nm, and (d) membrane-supported NLSVs at T = 100 K with I = 0.274 mA. Lateral thermal gradients ∇T_{top} and ∇T_{bottom} across the two FM/NM detector junctions are indicated.

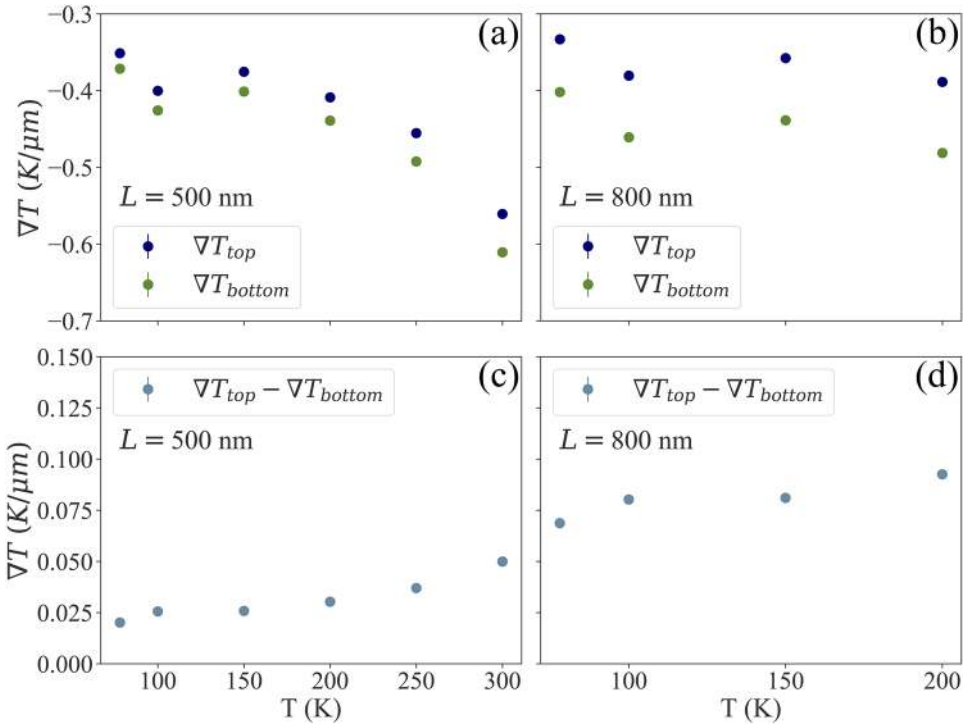

FIG. 6. For the L = 500 nm NLSV [(a) and (c)], the magnitude of the thermal gradient across the bottom detector contact (∇T_{bottom}, green symbols) is close to that of the thermal gradient across the top detector contact (∇T_{top}, dark purple symbols), as demonstrated by the subtracted difference between the two shown in panel (c). For the L = 800 nm NLSV [(b) and (d)], the magnitude of this difference is nearly three times larger. This represents a significant change in behavior between the two separation distances and device geometries that must be taken into account during our calculations of R_N.

but this remains a source of uncertainty. The input k for Si–N and Py uses values we have measured for these thin films using similar suspended Si–N thermal isolation platforms.[31,43,48] Figure 4 shows these k_{2D} values vs T for all three components. The Al values are calculated from the Wiedemann–Franz law, $k_e/\sigma = LT$, using the experimentally-determined Lorenz number, L, and σ determined from the measured first-order channel resistance for L = 500 nm (dark blue triangles) and L = 800 nm (pink triangles) NLSVs. No data are given for the L = 800 nm Al films above 200 K because no models were created at these temperatures. All k_{2D} show relatively weak dependence on T, and the small change in $k_{2D,Al}$ between the L = 500 nm and L = 800 nm devices is likely caused by variations in Al grain size caused by small variations in the channel width. Both Py and Si–N show similarly small k_{2D} due to the ~14× smaller thickness for Py.

Figure 5 shows contour plots of the resulting 2D FEM solutions for both membrane-suspended NLSVs. The black outlines show the location of metal features on the membrane. These model thermal spin injection, as is clear from panels (a) and (c) that show symmetric heating of the top and bottom of the NLSV structure. A closer view of the region of the membranes near the spin channel shown in panels (b) and (d) show the differing shapes of the FM2 nanowire and the resulting difference in temperature contours. Note that the low thermal conductance of the substrate leads to heating across the entire NLSV. The detailed views in Figs. 5(b) and 5(d) show significant thermal gradients even inside the nanoscale metallic features of both devices. As described in more detail elsewhere,[29] both the FM/NM junction between the detector and the spin channel, shown at the bottom, and the FM/NM junction at the voltage lead, shown at the top, produce a Nernst electric field. The in-plane thermal gradients at these locations, that drive these ANE contributions, are ∇T_{bottom} and ∇T_{top}. These ANE fields point in opposite directions with respect to the measurement contacts since one contact is held as positive and the other as negative. Thus, the measured Nernst electric field is given, after integrating Eq. (1) for the geometry of the NLSV, by

$$V_{\text{ANE}} = S_{\text{N}} t_{\text{Py}} (\nabla T_{\text{top}} - \nabla T_{\text{bottom}}), \tag{3}$$

where t_{Py} is the Py film thickness and for ∇T_{top} and ∇T_{bottom} is defined in Figs. 5(b) and 5(d).

Although slight nonlinearities can exist in the lateral thermal gradients across the detector contacts, we determine ∇T_{top} and ∇T_{bottom} by performing linear fits to the T vs x data in each region at the y-coordinate location at the center of the contact. We display the results in Fig. 6. Changing L and the contact width has little effect on ∇T_{top} but has a larger effect on ∇T_{bottom}. This is due to the interplay of the detector nanowire shape and the separation distance between the two FM strips.[49] The calculated value $\nabla T_{\text{top}} - \nabla T_{\text{bottom}}$ [Figs. 6(c) and 6(d)] shows a weak dependence on T, with a similar trend in both devices for corresponding T, although with larger values for the L = 800 nm NLSV. This difference is used to determine the ANE coefficient R_{N} from

$$R_{\text{N}} S_{\text{Py}} = -\frac{V_{\text{ANE}}}{t_{\text{Py}} (\nabla T_{\text{bottom}} - \nabla T_{\text{top}})}. \tag{4}$$

In Fig. 7, we see the dependence of R_{N} and $S_{\text{N}} = R_{\text{N}} S_{\text{Py}}$ on the base temperature T. Note that the S_{N} values shown in Fig. 7(b) do not include any assumption of values of the Seebeck coefficient, so

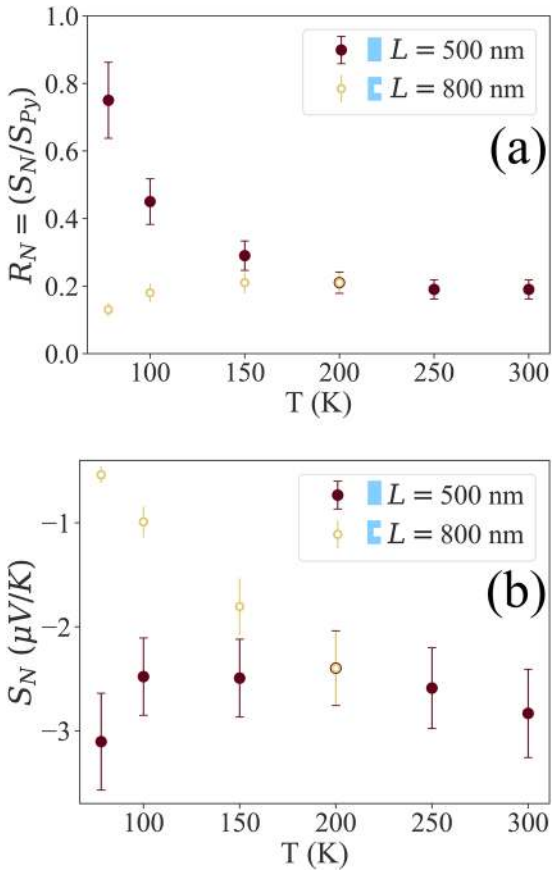

FIG. 7. (a) R_{N}, determined using values of S_{Py} taken from similar thin films. Values from the two NLSVs converge at T = 200 K. The divergence between values calculated from each device at T < 150 K is thought to be caused by the effect of the detector nanowire geometry on ∇T_{bottom} and the absolute Seebeck coefficient S_{Py}.[49] All error bars are dominated by the 15% error in t_{Py}. (b) S_{N} vs T for the two NLSVs.

they are the most direct measure of the size of Nernst signals in the NLSVs. The error bars shown are dominated by the ~15% uncertainty in t_{Py}. The two different NLSVs show quite different trends for S_{N} with T, with a nearly linear behavior for the L = 800 nm NLSV and relatively constant values for the L = 500 nm NLSV. We note that a nearly T-independent behavior is also seen in ρ_H for polycrystalline Py films of similar thickness.[8] Since S_{N} and ρ_{H} have been shown to be related via the Mott equation,[4] this weak T-dependence is reasonable.

Determining R_{N} requires knowledge of the absolute Seebeck coefficient of Py, and here, we have used values measured using similar Si–N membrane techniques[30] to estimate this number. Variations in thickness, geometry, or composition could alter the S_{Py} values somewhat and introduce an overall scaling error or modify the apparent T dependence. Further studies to understand the impact of these factors on the ANE are ongoing. However, for both R_{N} and S_{N} above 150 K, the values for both NLSVs agree well, and at 200 K, the two data points are coincident on this scale. R_{N}

= 0.2 around T = 200 K for both devices, which agrees with previous measurements of this value for Py.[2,11] However, it is immediately clear that the T dependence of both R_N and S_N is more significant than that of either $\nabla T_{top} - \nabla T_{bottom}$ or any of the k_{2D} values for the device components. We suspect that the apparent divergence of S_N between the L = 500 nm and L = 800 nm devices below T = 150 K is driven by changes in S_{Py} due to the constricted detector nanowire in the L = 800 nm device.[49] Similar geometrical constrictions in single-component metallic nanowires have been observed to give rise to thermoelectric voltages,[50–52] although open questions surround these thermoelectric size-effects. Aspects of our ongoing work are focused on probing geometric effects in ferromagnetic and other metallic nanowire systems.

IV. CONCLUSIONS

In summary, we presented evidence of T dependent S_N and R_N for Py measured with membrane-suspended metallic NLSVs. A relatively weak T-dependence for S_N in the simplest NLSV geometry is in line with expectations for ρ_H on similar Py films. We also show evidence of effects on ∇T and S_N due to device geometry. Further studies are underway to determine the effects of the constricted nanowire used in the L = 800 nm NLSV on S_{Py}.

ACKNOWLEDGMENTS

We thank D. Wesenberg for assistance and advice on fabrication techniques and finite element calculations, and we gratefully acknowledge the support from the NSF (Grant Nos. ECCS-1610904 and DMR-1709646). This work was performed, in part, at the Center for Integrated Nanotechnologies, an Office of Science User Facility operated for the US Department of Energy (DOE) Office of Science by Los Alamos National Laboratory (Contract No. DE-AC52-06NA25396) and Sandia National Laboratories (Contract No. DE-AC04-94AL85000). The bulk of this work was performed on lands traditionally held by the Cheyenne and Arapaho nations.

DATA AVAILABILITY

The data that support the findings of this study are available from the corresponding author upon reasonable request.

REFERENCES

[1] T. Seki, R. Iguchi, K. Takanashi, and K. Uchida, "Relationship between anomalous Ettingshausen effect and anomalous Nernst effect in an FePt thin film," J. Phys. D: Appl. Phys. **51**, 254001 (2018).
[2] T. C. Chuang, P. L. Su, P. H. Wu, and S. Y. Huang, "Enhancement of the anomalous Nernst effect in ferromagnetic thin films," Phys. Rev. B **96**, 174406 (2017).
[3] N. Nagaosa, J. Sinova, S. Onoda, A. H. MacDonald, and N. P. Ong, "Anomalous Hall effect," Rev. Mod. Phys. **82**, 1539–1592 (2010).
[4] Y. Pu, D. Chiba, F. Matsukura, H. Ohno, and J. Shi, "Mott relation for anomalous Hall and Nernst effects in $Ga_{1-x}Mn_xAs$ ferromagnetic semiconductors," Phys. Rev. Lett. **101**, 117208 (2008).
[5] T. Miyasato, N. Abe, T. Fujii, A. Asamitsu, S. Onoda, Y. Onose, N. Nagaosa, and Y. Tokura, "Crossover behavior of the anomalous Hall effect and anomalous Nernst effect in itinerant ferromagnets," Phys. Rev. Lett. **99**, 086602 (2007).
[6] Y. Q. Zhang, N. Y. Sun, R. Shan, J. W. Zhang, S. M. Zhou, Z. Shi, and G. Y. Guo, "Anomalous Hall effect in epitaxial permalloy thin films," J. Appl. Phys. **114**, 163714 (2013).
[7] Y. Q. Zhang, N. Y. Sun, W. R. Che, R. Shan, and Z. G. Zhu, "Origin of enhanced anomalous Hall effect in ultrathin Pt/permalloy bilayers," AIP Adv. **6**, 025214 (2016).
[8] Y. Omori, E. Sagasta, Y. Niimi, M. Gradhand, L. E. Hueso, F. Casanova, and Y. Otani, "Relation between spin Hall effect and anomalous Hall effect in 3*d* ferromagnetic metals," Phys. Rev. B **99**, 014403 (2019).
[9] H. Sharma, Z. Wen, K. Takanashi, and M. Mizuguchi, "Anomaly in anomalous Nernst effect at low temperature for $C1_b$-type NiMnSb half-Heusler alloy thin film," Jpn. J. Appl. Phys. **58**, SBBI03 (2019).
[10] P. Gautam, P. R. Sharma, Y. K. Kim, T. W. Kim, and H. Noh, "Temperature dependent anomalous Hall effect and anomalous Nernst effect in perpendicularly magnetized [CoSiB/Pt] multilayer film," J. Magn. Magn. Mater. **446**, 264–269 (2018).
[11] A. Slachter, F. L. Bakker, and B. J. van Wees, "Anomalous Nernst and anisotropic magnetoresistive heating in a lateral spin valve," Phys. Rev. B **84**, 020412 (2011).
[12] S. Y. Huang, W. G. Wang, S. F. Lee, J. Kwo, and C. L. Chien, "Intrinsic spin-dependent thermal transport," Phys. Rev. Lett. **107**, 216604 (2011).
[13] S. Hu and T. Kimura, "Anomalous Nernst-Ettingshausen effect in nonlocal spin valve measurement under high-bias current injection," Phys. Rev. B **87**, 014424 (2013).
[14] J.-E. Wegrowe, H.-J. Drouhin, and D. Lacour, "Anisotropic magnetothermal transport and spin Seebeck effect," Phys. Rev. B **89**, 094409 (2014).
[15] F. Brandl and D. Grundler, "Fabrication and local laser heating of freestanding $Ni_{80}Fe_{20}$ bridges with Pt contacts displaying anisotropic magnetoresistance and anomalous Nernst effect," Appl. Phys. Lett. **104**, 172401 (2014).
[16] P. Bougiatioti, C. Klewe, D. Meier, O. Manos, O. Kuschel, J. Wollschläger, L. Bouchenoire, S. D. Brown, J.-M. Schmalhorst, G. Reiss, and T. Kuschel, "Quantitative disentanglement of the spin Seebeck, proximity-induced, and ferromagnetic-induced anomalous Nernst effect in normal-metal–ferromagnet bilayers," Phys. Rev. Lett. **119**, 227205 (2017).
[17] J. Holanda, O. Alves Santos, R. O. Cunha, J. B. S. Mendes, R. L. Rodríguez-Suárez, A. Azevedo, and S. M. Rezende, "Longitudinal spin Seebeck effect in permalloy separated from the anomalous Nernst effect: Theory and experiment," Phys. Rev. B **95**, 214421 (2017).
[18] U. Martens, T. Huebner, H. Ulrichs, O. Reimer, T. Kuschel, R. R. Tamming, C.-L. Chang, R. I. Tobey, A. Thomas, M. Münzenberg, and J. Walowski, "Anomalous Nernst effect and three-dimensional temperature gradients in magnetic tunnel junctions," Commun. Phys. **1**, 65 (2018).
[19] M. Johnson, "Spin accumulation in gold films," Phys. Rev. Lett. **70**, 2142–2145 (1993).
[20] F. J. Jedema, A. T. Filip, and B. J. van Wees, "Electrical spin injection and accumulation at room temperature in an all-metal mesoscopic spin valve," Nature **410**, 345–348 (2001).
[21] Y. Ji, A. Hoffmann, J. S. Jiang, and S. D. Bader, "Spin injection, diffusion, and detection in lateral spin-valves," Appl. Phys. Lett. **85**, 6218–6220 (2004).
[22] S. O. Valenzuela and M. Tinkham, "Spin-polarized tunneling in room-temperature mesoscopic spin valves," Appl. Phys. Lett. **85**, 5914–5916 (2004).
[23] Y. Niimi, D. Wei, H. Idzuchi, T. Wakamura, T. Kato, and Y. Otani, "Experimental verification of comparability between spin-orbit and spin-diffusion lengths," Phys. Rev. Lett. **110**, 016805 (2013).
[24] G. E. W. Bauer, E. Saitoh, and B. J. van Wees, "Spin caloritronics," Nat. Mater. **11**, 391 (2012).
[25] S. R. Boona, R. C. Myers, and J. P. Heremans, "Spin caloritronics," Energy Environ. Sci. **7**, 885–910 (2014).
[26] C. H. Back, G. E. W. Bauer, and B. L. Zink, "Special issue on spin caloritronics," J. Phys. D: Appl. Phys. **52**, 230301 (2019).
[27] F. L. Bakker, A. Slachter, J.-P. Adam, and B. J. van Wees, "Interplay of Peltier and Seebeck effects in nanoscale nonlocal spin valves," Phys. Rev. Lett. **105**, 136601 (2010).

[28]F. Casanova, A. Sharoni, M. Erekhinsky, and I. K. Schuller, "Control of spin injection by direct current in lateral spin valves," Phys. Rev. B **79**, 184415 (2009).
[29]R. K. Bennet, A. Hojem, and B. L. Zink, "Thermal gradients and anomalous Nernst effects in membrane-supported nonlocal spin valves," Phys. Rev. B **100**, 104404 (2019).
[30]A. Hojem, D. Wesenberg, and B. L. Zink, "Thermal spin injection and interface insensitivity in permalloy/aluminum metallic nonlocal spin valves," Phys. Rev. B **94**, 024426 (2016).
[31]A. D. Avery, S. J. Mason, D. Bassett, D. Wesenberg, and B. L. Zink, "Thermal and electrical conductivity of approximately 100-nm permalloy, Ni, Co, Al, and Cu films and examination of the Wiedemann-Franz law," Phys. Rev. B **92**, 214410 (2015).
[32]R. W. Powell, C. Y. Ho, and P. E. Liley, "Thermal conductivity of selected materials," National Bureau of Standards, NSRDS No. 8, 1966.
[33]A. D. Avery, M. R. Pufall, and B. L. Zink, "Observation of the planar Nernst effect in permalloy and nickel thin films with in-plane thermal gradients," Phys. Rev. Lett. **109**, 196602 (2012).
[34]M. Schmid, S. Srichandan, D. Meier, T. Kuschel, J.-M. Schmalhorst, M. Vogel, G. Reiss, C. Strunk, and C. H. Back, "Transverse spin Seebeck effect versus anomalous and planar Nernst effects in permalloy thin films," Phys. Rev. Lett. **111**, 187201 (2013).
[35]D. Meier, D. Reinhardt, M. Schmid, C. H. Back, J.-M. Schmalhorst, T. Kuschel, and G. Reiss, "Influence of heat flow directions on Nernst effects in Py/Pt bilayers," Phys. Rev. B **88**, 184425 (2013).
[36]D. Meier, D. Reinhardt, M. van Straaten, C. Klewe, M. Althammer, M. Schreier, S. T. B. Goennenwein, A. Gupta, M. Schmid, C. H. Back, J.-M. Schmalhorst, T. Kuschel, and G. Reiss, "Longitudinal spin Seebeck effect contribution in transverse spin Seebeck effect experiments in Pt/YIG and Pt/NFO," Nat. Commun. **6**, 8211 (2015).
[37]A. Slachter, F. L. Bakker, J.-P. Adam, and B. J. van Wees, "Thermally driven spin injection from a ferromagnet into a non-magnetic metal," Nat. Phys. **6**, 879 (2010).
[38]M. Erekhinsky, F. Casanova, I. K. Schuller, and A. Sharoni, "Spin-dependent Seebeck effect in non-local spin valve devices," Appl. Phys. Lett. **100**, 212401 (2012).
[39]S. Hu, H. Itoh, and T. Kimura, "Efficient thermal spin injection using CoFeAl nanowire," NPG Asia Mater. **6**, e127 (2014).
[40]K. Yamasaki, S. Oki, S. Yamada, T. Kanashima, and K. Hamaya, "Spin-related thermoelectric conversion in lateral spin-valve devices with single-crystalline Co_2FeSi electrodes," Appl. Phys. Express **8**, 043003 (2015).
[41]A. Pfeiffer, S. Hu, R. M. Reeve, A. Kronenberg, M. Jourdan, T. Kimura, and M. Kläui, "Spin currents injected electrically and thermally from highly spin polarized Co_2MnSi," Appl. Phys. Lett. **107**, 082401 (2015).
[42]G.-M. Choi, C.-H. Moon, B.-C. Min, K.-J. Lee, and D. G. Cahill, "Thermal spin-transfer torque driven by the spin-dependent Seebeck effect in metallic spin-valves," Nat. Phys. **11**, 576 (2015).
[43]R. Sultan, A. D. Avery, J. M. Underwood, S. J. Mason, D. Bassett, and B. L. Zink, "Heat transport by long mean free path vibrations in amorphous silicon nitride near room temperature," Phys. Rev. B **87**, 214305 (2013).
[44]S. Hu, X. Cui, T. Nomura, T. Min, and T. Kimura, "Nonreciprocity of electrically excited thermal spin signals in CoFeAl-Cu-Py lateral spin valves," Phys. Rev. B **95**, 100403 (2017).
[45]S. Kasai, S. Hirayama, Y. K. Takahashi, S. Mitani, K. Hono, H. Adachi, J. Ieda, and S. Maekawa, "Thermal engineering of non-local resistance in lateral spin valves," Appl. Phys. Lett. **104**, 162410 (2014).
[46]J. T. Batley, M. C. Rosamond, M. Ali, E. H. Linfield, G. Burnell, and B. J. Hickey, "Spin relaxation through Kondo scattering in Cu/Py lateral spin valves," Phys. Rev. B **92**, 220420 (2015).
[47]MATLAB and Partial Differential Equations Toolbox Release (The MathWorks, Inc., Natick, MA, USA, 2018).
[48]R. Sultan, A. D. Avery, G. Stiehl, and B. L. Zink, "Thermal conductivity of micromachined low-stress silicon-nitride beams from 77 to 325 K," J. Appl. Phys. **105**, 043501 (2009).
[49]R. K. Bennet, "2D confinement of thermal gradients in metallic non-local spin valves," Ph.D. thesis, University of Denver, 2020.
[50]P. Zolotavin, C. I. Evans, and D. Natelson, "Substantial local variation of the Seebeck coefficient in gold nanowires," Nanoscale **9**, 9160–9166 (2017).
[51]G. P. Szakmany, A. O. Orlov, G. H. Bernstein, and W. Porod, "Single-metal nanoscale thermocouples," IEEE Trans. Nanotechnol. **13**, 1234–1239 (2014).
[52]N. B. Duarte, G. D. Mahan, and S. Tadigadapa, "Thermopower enhancement in nanowires via junction effects," Nano Lett. **9**, 617 (2009).